PHYSICAL REVIEW E **70**, 036501 (2004)

Mechanism of electron multipacting with a long-bunch proton beam

L. Wang, M. Blaskiewicz, J. Wei, and W. T. Weng
Brookhaven National Laboratory, Upton, New York 11973-5000, USA

K. Ohmi
High Energy Accelerator Research Organization, Tsukuba, Ibaraki 305-0801, Japan

R. Macek
Los Alamos National Laboratory, Los Alamos, New Mexico 87545-1663, USA

(Received 20 January 2004; published 29 September 2004)

The energy gain and motion of electrons can quantitatively describe the mechanism of electron multipacting in a long-bunched proton machine. Strong multipacting usually happens around the bunches' tails due to the high energy of electrons when they hit the chamber surface. We investigated several important parameters of electron multipacting, proving that it is sensitive to the beam's intensity, the shape of its longitudinal profile, its transverse size, the secondary emission yield, and the energy at peak secondary emission yield. Our analyses, simulations, and experiments are all in agreement.

DOI: 10.1103/PhysRevE.70.036501 PACS number(s): 29.27.Bd, 29.20.Lq

INTRODUCTION

The problem of transverse instability and beam loss due to electron-proton interactions has long persisted. It was first observed at the Budker Institute of Nuclear Physics (INP) Proton Storage Ring (PSR) [1]. Shortly thereafter, electron cloud- and beam-induced multipacting was found at CERN Intersecting Storage Rings (ISR) [2,3] during the coasting beam operation, and was cured with clearing electrodes. More recently, an electron cloud caused transverse instability in a bunched proton beam in the Proton Storage Ring at Los Alamos National Laboratory (LANL PSR) [4,5]. Similar instability, seemingly due to electron and proton interactions, occurred at the Brookhaven National Laboratory Alternating Gradient Synchrotron booster [6]. It was also reported in the KEK Photo Factory (PF) [7,8], KEK B Factory [9], Stanford Linear Accelerator Center PEP-II [10], Beijing Electron Positron Collider [11], and the European Organization for Nuclear Research Proton Synchrotron (PS) and Super Proton Synchrotron (SPS) [12,13]. Gröbner suggested that beam-induced multipacting causes an electron cloud to accumulate inside the vacuum chamber [14,15]. It then interacts with the proton or positron beam and hence destabilizes it. Experimental observations of electron-cloud instabilities suggest that they differ distinctively for "short bunches" where multibunch multipacting is expected to be important (the PS, SPS, and B factories), and "long bunches" where single-bunch, trailing-edge multipacting is probably dominant; the mechanism of induction also seems to differ.

In this article, we discuss electron-cloud buildup in a long proton machine. The PSR is the one in which strong electron-cloud instability was reported. Two qualitative mechanisms were offered to explain it [5,16]. One of our objectives was to quantify the mechanism of multipacting in the long proton beam. Previous studies analyzed electron motion and energy gain [17,18]; however, we made a more detailed analysis of electron motion under the beam's space-charge force and dipole magnetic fields. Knowledge of the electron's motion and energy when it hits the chamber's surface is most helpful in elucidating the mechanism of electron multipacting. We confirmed our analysis with the simulation code CLOUDLAND [19]. Our results gave us a clearer physical basis to explain the electron-cloud buildup in a long-bunch machine, which may answer some questions that the numerical methods could not resolve.

Furthermore, by investigating the factors affecting multipacting individually instead of considering them together, we can clearly delineate the effect of each one. Many studies explored electron-cloud buildup in long-bunch proton machines using numerical methods [17,18,20–22]. We know from PSR experiments and the simulations described in this paper that the buildup depends on several factors, such as the shape of the beam's longitudinal and, transverse profiles, intensity, chamber size, and secondary emission yield (SEY). Earlier simulations did not examine many variations of these parameters; we undertook a more systematic examination that we compare with experimental results. A wealth of data from the PSR can be used to compare with these simulations to benchmark the code. The combination of our analysis of electron motion and simulation of electron-cloud buildup might give us a better understanding of the physics of electron multipacting.

This paper is organized as follows. First, we introduce the SEY and physics model used in the code CLOUDLAND. Second, we explore electron motion under the beam's space-charge force and dipole magnetic field. Long bunches can trap electrons that are emitted or exist before the bunches' centers. On the other hand, electrons emitted from the chamber surface after the center of a proton bunch move straight to the opposite wall's surface. Accordingly, no electrons are lost before the bunch's center, partly explaining why multipacting always occurs at the bunch's tail. The electron's gain in energy is analyzed as a function of the beam's longitudinal profile, its transverse size, and the chamber's size. We define one very important factor, the longitudinal beam profile factor, according to which the gain in electron energy is usually

TABLE I. Simulation parameters for the SNS and PSR.

Parameter	Description	SNS	PSR
E(GeV)	Beam energy	1.9	1.75
C(m)	Circumference	248	90
N_p	Beam intensity	2.05×10^{14}	5×10^{13}
$a_x, a_y/\sigma_x, \sigma_y$(mm)	Transverse beam size	28, 28	10, 10
τ_b(ns)	Bunch length	700	250
b(cm)	Beam pipe radius	10	5
P_l	Proton loss rate per turn	1.1×10^{-6}	4.0×10^{-6}
Y	Proton-electron yield	100	100

bigger at the bunch's tail, thereby accounting for the mechanism of the so-called "trailing-edge multipactor." Third, we discuss a few significant parameters related to electron multipacting that we investigated and simulated in greater detail.

SEY AND THE PHYSICS MODEL

Oak Ridge National Laboratory is constructing a Spallation Neutron Source (SNS), equipped with high-intensity proton storage. As examples, we use the SNS ring and PSR beam in this study. Table I shows the beams' parameters. The SNS beam is assumed to be cylindrical with uniform distribution in the transverse plane, and the PSR beam is Gaussian.

The main source of primary electrons varies from one storage ring to another. Photon electrons are one of the main sources in machines with a high relativistic factor. The energy of the SNS and PSR beams is low; therefore, photoelectrons are not their main source of electrons. Rather, electrons generated at the stripping foil in the ring's injection region are one of the main sources. A special electron collector and clearing electrode are installed in the SNS's injection region. However, stripped electrons were not a concern for this research. The other two main sources of electrons that we discuss arise from beam loss at the chamber's surface and from the ionization of residual gas.

A major unknown factor is the number of electrons created at the wall. In the PSR, this number at any given location is uncertain by at least two orders of magnitude. It is difficult to reliably estimate the electron yield from proton losses because we need to know the exact grazing angle of incidence for the lost protons, and the places where they are lost; there are no experimental data with the required detail on either parameter. Conceptually, the number of initial electrons created at the wall might be treated as proportional to the instantaneous line density of protons in the region of interest (assuming the losses are proportional to line density) with the proportionality constant a free parameter to be fixed by comparing the simulations to one set of experimental data. In Table I, we assumed a uniform rate of proton loss along the ring (far from true in the real machine), and a proton-electron yield of 100 from comparing the simulations and experimental data from the PSR.

When these electrons, generated from beam loss or gas ionization, hit the beam chamber's surface after a period of transit, they produce more electrons, called secondary electrons. Their emission is important for the buildup of the electron cloud. Secondary electrons include three types: backscattered electrons, rediffused electrons, and true secondary electrons [23–26]. The secondary emission yield is defined as the fraction of the number of electrons emitted from the metal's surface to the total number of incident electrons. When the SEY is larger than unity, the number of electrons increases exponentially. This avalanche phenomenon is called multipacting.

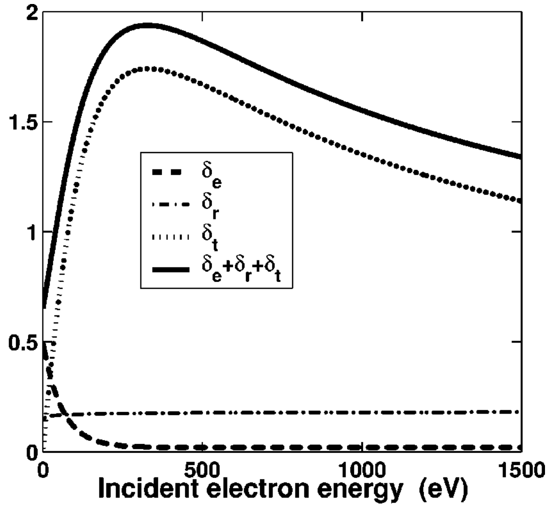

FIG. 1. Secondary emission yield with normal incident angle.

Figure 1 shows the SEY used for the simulation. The material of the SNS chamber is stainless steel coated with titanium nitride (TiN). The true secondary parameters are based on one of the experimental results from CERN. Cimino *et al.* recently showed that the yield of reflected electrons with zero energy is close to 1 [27]. Therefore, the reflected component plays a major role in the SEY at low energies. Multipacting strongly depends on the SEY's parameters. In a real storage ring, the measured SEY parameters should be applied in estimating electron multipacting because of its strong dependence on them.

The simulation program, CLOUDLAND that we used is a three-dimensional particle-in-cell (PIC) code [19]. It includes the three-dimensional electron and proton space charge, beam-electron interaction, and various magnetic and electric fields. A primary electron is emitted when a lost proton hits the wall. The electrons move under the beam and its space charge. Inside magnets, the magnetic field should also be included in the calculations. When an electron hits the vacuum chamber's surface, it generates secondary electrons. A statistical distribution generator obeying the experimental results controls the SEY, energy, and emission angle. Similarly, the secondary electrons may generate tertiary electrons. Because the SEY strongly depends on the energy of the incident electrons, multipacting is closely related to electron motion.

PARTICLE MOTION

The primary electrons are produced by beam loss at the chamber's surface and ionization at the beam's position. If an electron can oscillate many times under the beam force during the passage of one bunch, then the bunch is called a long bunch. Assuming the bunch length is $2\hat{z}$ and the average frequency of electron oscillation is $\overline{\omega}$, a long bunch should satisfy

$$\frac{\hat{z}\overline{\omega}}{\pi\beta c} \geqslant 1, \tag{1}$$

where β is the velocity of the proton normalized by the speed of light c. Both the SNS and PSR are long beams, wherein the trapped electrons can oscillate for more than 50 periods during the bunch's passage.

Magnetic-field-free region

In the magnetic-field-free region, the electrons move under the space-charge fields of the proton beam and between other electrons. The space-charge field of the electron cloud can be neglected during the beam's passage because the neutralization factor is small except at the bunch's tail, where strong multipacting usually happens. For the long proton bunch, we can also neglect the longitudinal space-charge field due to potential variations in longitudinal direction because of the slow variation in, and the symmetry of, the longitudinal beam profile that traps the particles longitudinally. Therefore, the electrons mainly move under the beam's transverse fields.

The SNS beam's transverse profile resembles a square with a uniform distribution resulting from correlated painting during injection. Including the space charge causes rapid diffusion in the azimuthal direction, yielding a round shape [28]. A cylindrical transverse profile is assumed in this paper to approximate the SNS beam's real distribution.

For a cylindrical beam with a uniform transverse distribution, the space-charge field is

$$E_r(t) = \begin{cases} \dfrac{\lambda(t)}{4\pi\varepsilon_0}\dfrac{2}{r} & (r > a), \\[2ex] \dfrac{\lambda(t)}{4\pi\varepsilon_0}\dfrac{2r}{a^2} & (r < a), \end{cases} \tag{2}$$

where $\mu_0 = 4\pi \times 10^{-7}$ H/m is called the permeability of vacuum, $\varepsilon_0 = 10^{-9}/36\pi$ F/m is known as the permittivity of vacuum, λ is the beam's line density, and a is the transverse beam size. The electron moves slowly in the longitudinal direction (beam's direction) due to the weak longitudinal beam's space charge field, and rotates in the azimuthal direction with constant angular velocity that depends on the initial condition. Since the radial motion is uncoupled from that in the other directions, the nonlinear Hamiltonian of the radial motion is obtained as

$$H = \frac{p^2}{2m} + eU(r,t), \tag{3}$$

with

$$U(r,t) = \begin{cases} \dfrac{\lambda(t)}{4\pi\varepsilon_0}\left(1 + 2\ln\dfrac{r}{a}\right) & (r > a), \\[2ex] \dfrac{\lambda(t)}{4\pi\varepsilon_0}\dfrac{r^2}{a^2} & (r < a). \end{cases} \tag{4}$$

The electron radial motion is a "nearly periodic oscillation" with a slow time dependence given by the function $\lambda(t)$. Assuming constant λ, the electron will make exact periodical nonlinear oscillations. In the maximum oscillation amplitude r_{amp}, the kinetic energy is zero. To calculate the period of nonlinear oscillations, this is integrated over one-fourth of the oscillation period:

$$T = 4.0\int_0^{r_{amp}} \frac{dr}{\upsilon(r)} = 4.0\int_0^{r_{amp}} \frac{dr}{\sqrt{2\Phi e/m}}, \tag{5}$$

with

$$\Phi(r) = \begin{cases} \dfrac{\lambda}{2\pi\varepsilon_0}\ln\dfrac{r_{amp}}{r} & (r > a,\ r_{amp} > a), \\[2ex] \dfrac{\lambda}{4\pi\varepsilon_0}\left(1 + 2\ln\dfrac{r_{amp}}{a} - \dfrac{r^2}{a^2}\right) & (r \leqslant a,\ r_{amp} > a), \\[2ex] \dfrac{\lambda}{4\pi\varepsilon_0 a^2}(r_{amp}^2 - r^2) & (r \leqslant r_{amp} \leqslant a), \end{cases} \tag{6}$$

where m is the mass of the electron. Substituting Φ of Eq. (6) for that of Eq. (5), the period of nonlinear motion is

$$T = \begin{cases} 4.0\sqrt{\dfrac{\pi\varepsilon_0 m}{\lambda e}}\left(\sqrt{2}a\arcsin\dfrac{1}{\sqrt{1 + 2\ln(r_{amp}/a)}} + \displaystyle\int_a^{r_{amp}} \dfrac{dr}{\sqrt{\ln(r_{amp}/r)}}\right) & (r_{\mathrm{amp}} > a), \\[3ex] 2\pi a\sqrt{\dfrac{2\pi\varepsilon_0 m}{\lambda e}} & (r_{\mathrm{amp}} \leqslant a). \end{cases} \tag{7}$$

The electrons produced by ionization at the beam have radial coordinates smaller than the beam's size. Therefore, they will oscillate under the linear force. However, electrons produced by loss at the beam's pipe will oscillate under the nonlinear force. Consequently, the oscillator frequency depends on the radial coordinate when $r_{amp} > a$ due to the effect of the nonlinear force.

If the beam's line density $\lambda(t)$ does not change much within one period of electron oscillation,

$$\frac{1}{\omega_e^2}\frac{d\omega_e}{dt} \ll 1, \tag{8}$$

there is an adiabatic invariant which is defined with canonical variables p and q as

$$J = \oint p\,dq. \tag{9}$$

For the SNS beam, condition (8) is satisfied except during the first and last 20 ns of the bunch's 700 ns pulse. Therefore, the adiabatic invariant exists during most of the beam passage.

For a given oscillation amplitude $r_{amp}, p(r)$ can be written as

$$p(r,t) = \sqrt{2em[U(r_{amp},t) - U(r,t)]}. \tag{10}$$

Substituting Eqs. (4) and (10) into Eq. (9), we get the motion invariant

$$J = \begin{cases} \dfrac{\pi r_{amp}^2}{a}\sqrt{\dfrac{me\lambda}{2\pi\varepsilon_0}} & (r_{amp} \leq a), \\ 4a\sqrt{\dfrac{me\lambda}{2\pi\varepsilon_0}}\left(\dfrac{\sqrt{2}}{2}x^{1/2} + \dfrac{1+2x}{2}\arctan\dfrac{1}{\sqrt{2x}} + \dfrac{\sqrt{2}}{a}\displaystyle\int_a^{r_{amp}}\sqrt{\ln\frac{r_{amp}}{r}}dr\right) & (r_{amp} > a), \end{cases} \tag{11}$$

where $x = \ln(r_{amp}/a)$.

For a "smooth" longitudinal beam profile (continuous with its derivative), the variation in the electron's oscillation amplitude due to the changes in beam density during the bunch's passage can be calculated according to Eq. (11); Fig. 2 gives an example of such a calculation, and of frequency estimated by Eq. (7). The estimated amplitude, shown as the dashed solid black line, agrees well with the particle's numerically simulated oscillation amplitude. The oscillation frequency, which depends on the amplitude and beam density, ranges from 20 to 140 MHz.

For a Gaussian beam, the linear oscillation frequency under the beam force is

$$f_{x,y} = \frac{1}{2\pi}\sqrt{\frac{2r_e\lambda c^2}{\sigma_{x,y}(\sigma_x + \sigma_y)}}. \tag{12}$$

The oscillation frequency of electrons varies during the beam's passage. Consequently, the proton beam oscillates coherently at a frequency range different from the above incoherent oscillation frequency by a factor that depends on neutralization caused by coupling between electrons and the proton beam. Therefore, electron-proton instabilities can be distinguished from the conventional impedance-caused instability with its resonant frequency width that depends on the beam. The peak beam spectrum is roughly proportional to

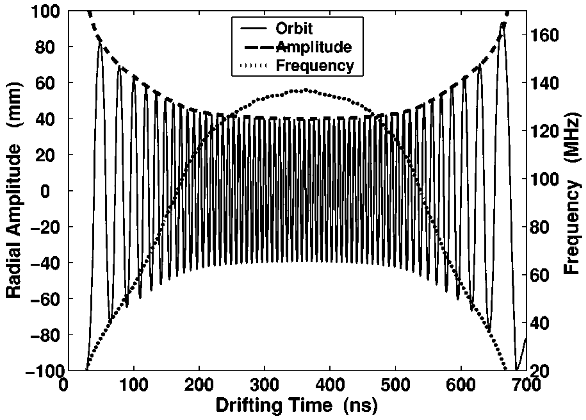

FIG. 2. Amplitude and frequency of oscillation. The dashed black line is the estimated amplitude.

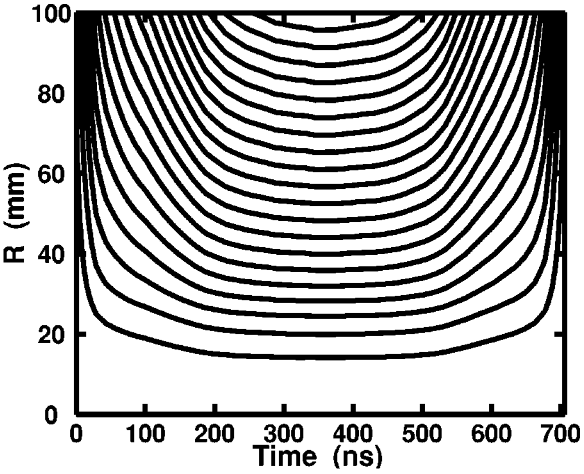

FIG. 3. Contour plot of the oscillation amplitude resulting from adiabatic invariance for the SNS beam.

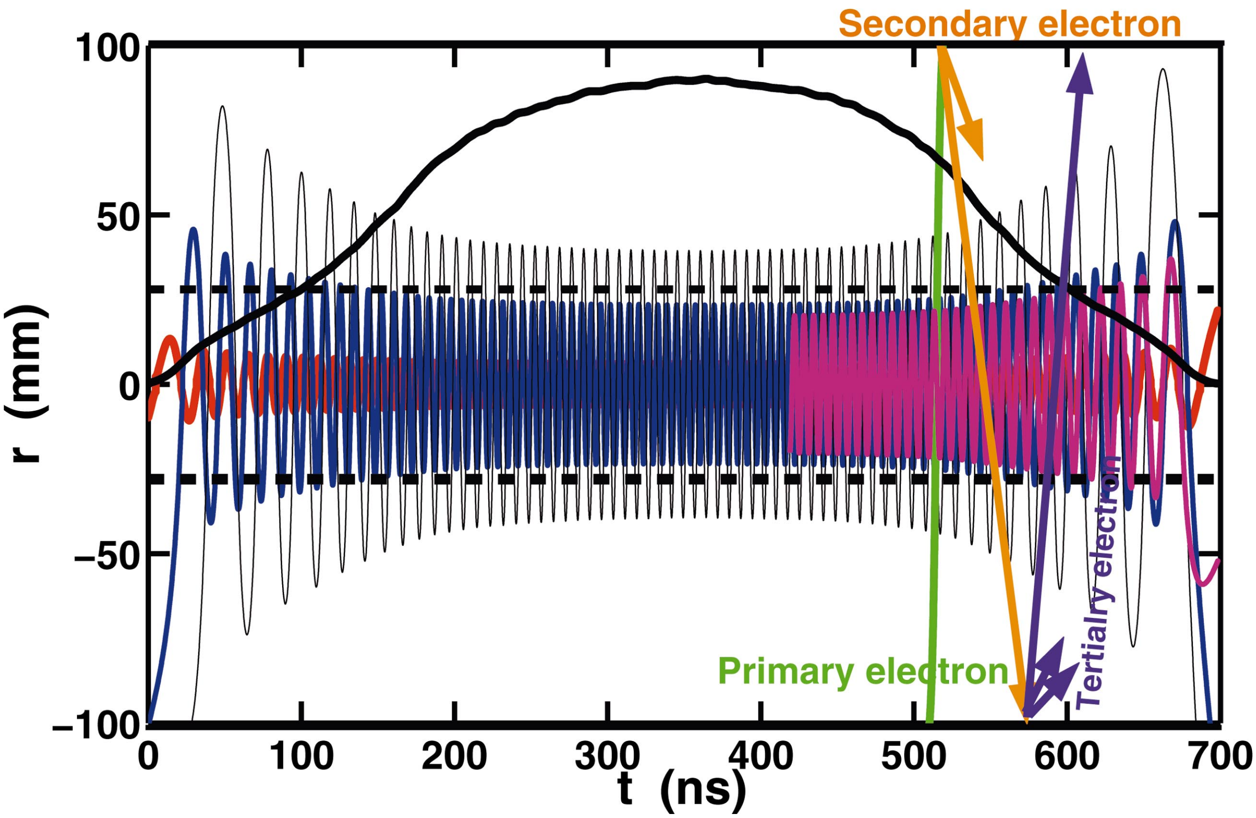

FIG. 4. (Color) Typical orbits of various electrons in the SNS beam; the bold solid line shows the shape of the longitudinal beam profile and the dashed black lines show its transverse size. The blue and red lines show the orbits of surviving electrons from the last bunch gap. They are trapped inside the beam during its passage and can cause beam instabilities. The solid back line shows the orbit of an electron that is emitted at the chamber surface between the bunch's head and center. It oscillates with large amplitude and is lost between the bunch's the center and tail. The green line shows an electron that is emitted at the chamber's surface between bunch center and tail. It is important for multipacting, as it generates secondary and tertiary electrons. The pink line shows the orbit of an electron generated by ionization.

$\sqrt{N_p}$ [4,29], and close to the incoherent frequency given by Eq. (7) because the neutralization factor is small. Hence, Eq. (7) and Eq. (12) can be used to estimate the instability spectrum.

Figure 3 shows the amplitude contours calculated from the adiabatic invariant for the SNS beam's profile, and Fig. 4 shows the typical orbit of electrons obtained by the CLOULDLAND program; they are consistent. Therefore, we drew the following conclusions.

(1) All electrons remaining inside the chamber before the approaching bunch (electrons surviving from the last bunch gap) can be trapped inside the beam during the bunch's passage and released at its end. Figure 4 depicts examples of such electron motions. The blue line shows that electrons surviving from the last bunch gap with oscillation amplitudes about the chamber's radius can still be trapped inside the beam. They are dynamically important, causing beam instability because huge numbers of them can be deeply trapped inside it. They have a weak effect on multipacting due to their long-term trapping and low energy at the chamber's surface during the passage of the bunch gap.

(2) The electrons emitted at the pipe's surface between the bunch's head and center will oscillate during the beam's passage and hit the chamber wall after the bunch center at the moment

$$t_{hit} \approx t_{emission} + 2(t_{bunchcenter} - t_{emission}) \tag{13}$$

due to the symmetry of the beam's profile. The earlier the electron is emitted, the later it hits the wall. Only electrons emitted at the bunch head could be deeply trapped inside the beam. More than 95% of primary electrons oscillate with amplitude bigger than the beam's size (Fig. 3). The thin black line in Fig. 4 is an example of such an electron's orbit.

(3) The electrons produced at the beam by ionization can be trapped inside it until the whole bunch passes them. The pink line in Fig. 4 gives the orbit of such an electron. These electrons have similar effects as the electrons surviving from the last bunch gap.

(4) The electrons emitted at the chamber's surface between the bunch's center and tail will move straight to the opposite chamber wall and produce secondary electrons because there the beam's profile has a negative derivative. The secondary electrons continue to cross the chamber until they hit the opposite surface to generate tertiary electrons. Electrons created at the wall between the bunches' center and tail are the only source of multipacting due to their having a short transit time and sufficient energy when they hit the chamber's surface at the bunch tail, as we discuss below. We call these electrons multipacting electrons; all other electrons

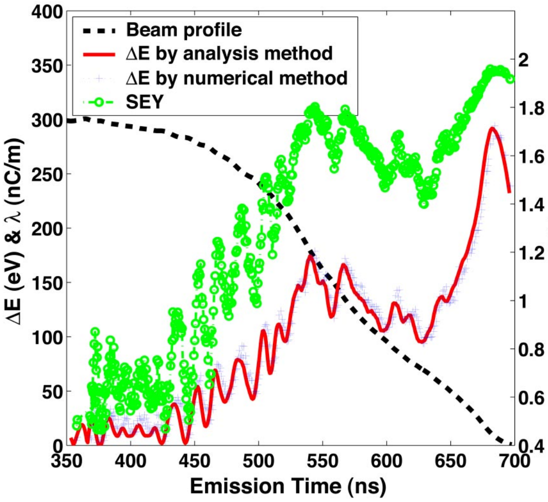

FIG. 5. (Color online) Energy gain and SEY of multipacting electrons.

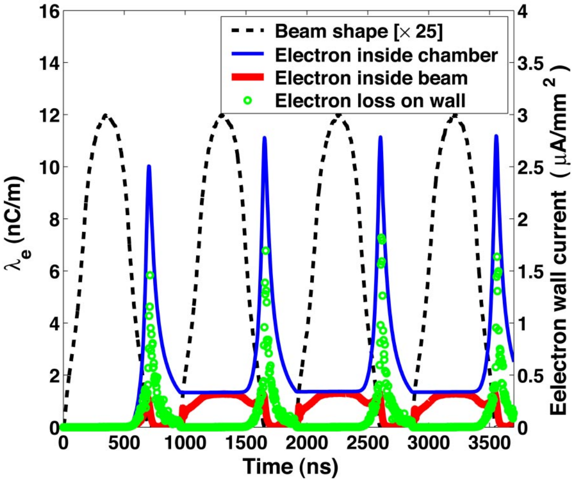

FIG. 6. (Color online) Electron-cloud buildup in the SNS drift region, showing the beam's longitudinal profile; the electron cloud's line density inside the chamber, representing the total number of electrons and hence multipacting; the electron line density inside the beam, which drives beam instabilities; and the current density of electrons striking the wall, which can be used to compare with experiment results.

as described in the above three paragraphs are termed trapped electrons. The green line in Fig. 4 plots the orbit of a multipacting electron. For the SNS beam, a multipacting electron can hit the chamber surface about 30 times during the period from bunch's center to its tail. On average, an electron takes 10 ns to strike the surface once.

(5) During the bunch gap, an electron may hit the chamber surface several times, which is less than four times for the SNS beam, and its energy is low due to the lack of acceleration from the beam. Therefore, there is no multipacting at the bunch gap. In fact, the space charge of the electron cloud ensures its rapid decay during the passage of the bunch gap.

If the transverse beam distribution is round Gaussian, the potential of the beam corresponding to Eq. (4) becomes

$$U(r) = \frac{\lambda}{4\pi\varepsilon_0}\int_0^r \frac{2}{t}\left[1 - \exp\left(-\frac{t^2}{2\sigma^2}\right)\right]dt. \qquad (14)$$

Similarly, we obtain the relationship of the electron's oscillation amplitudes as in Eq. (9). The PSR beam has an approximately Gaussian distribution transversely. Studies show that electrons can hit the chamber wall's surface only after the bunch center. Therefore, multipacting can occur only after it. These conclusions drawn for a beam with uniform transverse distribution also apply to a Gaussian beam.

The yield of primary electron emission depends on the rate of beam loss and vacuum pressure. In a real machine, the yield of electrons by beam loss is at least one order of magnitude larger than that by ionization. Further, electrons generated by ionization cannot excite multipacting due to their long-term trapping by the beam. Hence, we ignore electrons formed by ionization, focusing only on electrons yielded by beam loss.

Electrons emitted from the chamber's surface between the bunch center and tail are the only source of multipacting. For a multipacting electron, its energy gain from the beam when it hits the chamber surface is (Appendix A)

$$\Delta E = -\frac{1}{2}\beta c\sqrt{\frac{me}{2\pi\varepsilon_0}}\frac{\partial\lambda}{\partial z}\frac{1}{\sqrt{\lambda}}\left(a(2\zeta-1)\arcsin\frac{1}{\sqrt{\zeta}} + a\sqrt{2\ \ln\frac{b}{a}} + \sqrt{2}\zeta\int_a^b \frac{dr}{\sqrt{\ln(b/r)}} - \frac{1}{\sqrt{2}}\int_a^b \frac{1+2\ \ln(r/a)}{\sqrt{\ln(b/r)}}dr\right) \qquad (15)$$

with $\zeta = 1+2\ \ln(b/a)$. Figure 5 shows the good fit between the energy gain given by Eq. (15) and the numerical method. The electron's energy gain at the bunch's center is zero due to the zero derivative of the beam profile there, and is larger around its tail due to the beam's low line density around there. There are two peaks of energy gain around 550 ns where the derivative of the beam profile has two extrema; the maximum is 300 eV around the tail. The electron's initial energy when it is created is around a few eV's. Therefore, its energy when it strikes on the chamber surface is mainly decided by the gain from the beam. From the electron's energy at the wall surface, we can estimate the SEY. Figure 5 shows the SEY at different times. We conclude from the estimated SEY that multipacting starts at 450 ns and strengthens around 550 ns and the bunch tail due to the high energy there. Therefore, the energy gain can clearly delineate when the multipacting starts and when it is strong. The transit time for an electron to cross the chamber given by Eq. (A6) can describe the multipacting frequency. The mechanism of multipacting can be quantitatively described by Eqs. (15) and (A6).

Figure 6 shows the simulated electron density and the current density at the wall during the first four turns in one of the drift regions of the SNS ring. The electron cloud begins to build up at 500 ns and strong multipacting occurs at the bunch's tail. This agrees with the data shown in Fig. 5. During the bunch's passage, the electron line density inside the beam is almost equal to the line density inside the vacuum chamber, meaning that all electrons remain inside the beam during this time. Figures 3 and 4 explain this process. Thus, all electrons surviving from the last bunch gap will be trapped inside the beam because their oscillation amplitude is smaller than the beam's transverse size. They interact with the beam and destabilize it. On the other hand, most electrons linger around the chamber wall's surface at the bunch's tail due to the strong multipacting. This is more clearly depicted in Fig. 7 by the transverse distribution of the electron cloud at different times. The electron cloud rapidly decays during the bunch gap due to the space-charge effect. The electron line density inside the beam is less than 2.0 nC/m (Fig. 6). The neutralization factor is smaller than 1% except in the bunch's head and tail, so that elsewhere the effect of the space-charge force on electrons can be neglected. The electron cloud saturates just after one turn due to its strong space-charge effect at the bunch gap.

Dipole magnetic field

In a strong dipole magnet, an electron can effectively move only along the vertical magnetic field lines. Its vertical motion is similar to the radial motion of an electron in the drift region. For example, the beam's vertical space-charge field can vertically trap electrons emitted before the bunch's center; electrons emitted from the chamber's surface around the bunch's tail can excite multipacting. Following the same procedure as in the drift region, we can assess the energy gain in a dipole magnet for a multipacting electron moving along the vertical magnetic field line located at horizontal coordinate X as (Appendix B)

$$\Delta E = -\frac{1}{2}c\beta\sqrt{\frac{me}{2\pi\varepsilon_0}}\frac{\partial\lambda}{\partial z}\frac{1}{\sqrt{\lambda}}(\mathcal{T}_1+\mathcal{T}_2+\mathcal{T}_3)\quad(|X<a|), \tag{16a}$$

$$\Delta E = -\frac{1}{2}c\beta\sqrt{\frac{me}{2\pi\varepsilon_0}}\frac{\partial\lambda}{\partial z}\frac{1}{\sqrt{\lambda}}\int_0^{\sqrt{b^2-X^2}}\frac{2b^2-X^2-y^2}{X^2}\left(\ln\frac{b^2}{X^2+y^2}\right)^{-1/2}dy\quad(|X|>a) \tag{16b}$$

where $\mathcal{T}_1$, $\mathcal{T}_2$, and $\mathcal{T}_3$ are given by Eqs. (B15)–(B17). Figure 8 shows the relationship of the electron's energy gain at the wall surface with the X coordinate. It peaks at the chamber's center, which equals the energy gain in the drift region given by Eq. (15), and decreases at both sides. Thus, multipacting in a dipole magnet depends on the horizontal coordinate. It is the strongest at the chamber's center and weakens with the increment of $|X|$. Note that the energy gain in the dipole magnet has the same dependence on the beam's line density as in the drift region.

IMPORTANT FACTORS IN MULTIPACTING AND BUILDUP

Multipacting strongly depends on the electron's energy when it hits the vacuum chamber's surface. Accordingly, multipacting is related to the particle's motion. Some important factors on multipacting and electron-cloud buildup are discussed next. The experimental results from LANL's PSR are compared with simulations and analyses. The examples in this section refer to the SNS beam unless otherwise specified.

Effects of the longitudinal beam profile and bunch length

Equations (15) and (16) show the effect of the beam's longitudinal profile on the electron's energy gain that is governed by the longitudinal beam's profile factor $\mathcal{F}_{profile}$:

$$\mathcal{F}_{profile} = -\frac{\partial\lambda}{\partial z}\frac{1}{\sqrt{\lambda}}. \tag{17}$$

The first part of the profile factor, the derivative of the line density, represents the difference in beam density between the moments of electron emission and of electron loss. The smaller the beam profile derivative, the smaller is the electron's energy gain. For a coasting beam, the energy gain is zero due to the zero derivative of beam density, and hence there is no multipacting. The transit time represents the secondary part in the profile factor. The transit time round the bunch's tail is usually longer due to the low density of the beam there, and hence the gain in energy is bigger, and is the mechanism whereby strong multipacting invariably happens at the bunch's tail (Fig. 5). The effect of the longitudinal beam profile was first studied at the PSR [30], followed by analysis [17] and simulations [20].

Adjusting the buncher's phase can change the bunch tail. In the PSR, the electron signal at the tail increases by 140% when the rf of the buncher phase changes from 281° to 301° due to the increasing shoulder on the tail [30]. A longer tail causes stronger multipacting there. However, the instability threshold simultaneously increases by only 26% [31]. The variation is small in electron clouds inside the beam during the passage of the bunch, proportional to the rate of growth of proton instability [32], because of the faster decay during the bunch gap in the strong multipacting case. Therefore, the measured electron signal at the bunch tail is sensitive to the bunch phase, but the instability is less sensitive.

Using the same beam profile as shown in Fig. 5, Pivi and Furman [20] artificially truncated the bunch tail while maintaining the same integrated beam charge. Their simulation showed that electron density can be reduced by a factor of

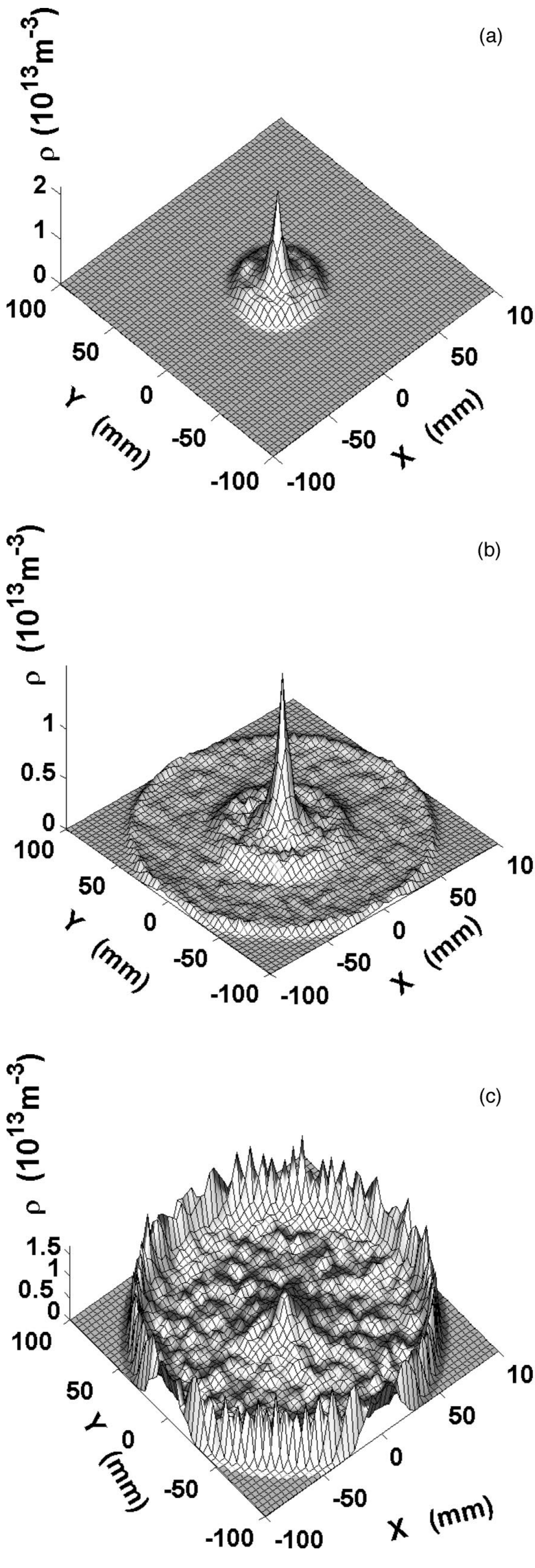

FIG. 7. Electron distributions in transverse section at the bunch center (top) 280 ns after the bunch center (middle), and in the bunch tail (bottom).

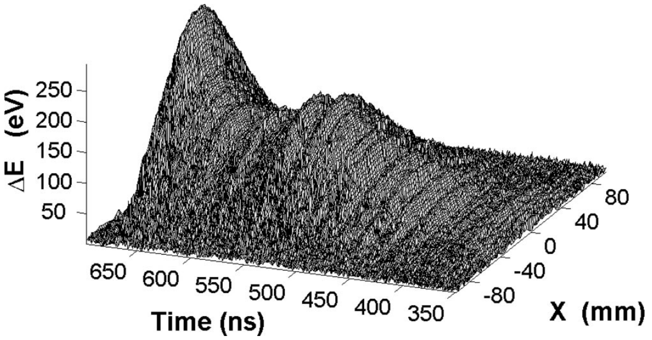

FIG. 8. Energy gain of multipacting electrons in the SNS's dipole magnets with $B_y = 7935$ G.

more than 100 when the beam's profile is cut at 500 ns. Comparing this finding with Fig. 5, cutting the bunch at 500 ns cuts off most of the multipacting area, thereby explaining these phenomena.

Figure 9 compares three assumed beam profiles, Gaussian, sinusoidal, and elliptical, all with the same integrated beam charge and secondary emission parameters as in Fig. 1. The figure also depicts their respective energy gain and the SEY. Comparing these parameters, the Gaussian profile is the worst. Multipacting happens at 375 ns, just 25 ns after the bunch's center, and the SEY is almost a constant value close to 2 for a long time. The elliptical profile is the best, with multipacting starting later at 600 ns and a smaller SEY. Therefore, the Gaussian profile has the largest peak electron density, 150 nC/m, while the elliptical profile has the minimum, of 1 nC/m [Fig. 9(d)]. A realistic beam profile has an electron density of about 12 nC/m, a little worse than the sinusoidal profile, which gives an electron density of 8 nC/m. These findings can be explained by the beam profile factor in Eq. (17). Therefore, the beam profile factor can be optimized to reduce electron multipacting.

Using the same secondary electron parameters, Fig. 10 gives the PSR beam profile, simulated electron energy gain, SEY, and electron-cloud build up in the PSR's drift region. We note that the distribution in the transverse plane of the PSR beam is approximately Gaussian. The electrons inside the beam must fall within $\sqrt{3}$ root mean square (rms) of the beam's size to conform to the uniform distribution. In plotting Fig. 10, the longitudinal beam profile factor was multiplied by a constant value to compare its shape with the energy gain. The two agree well because the Gaussian and uniform transverse beam profiles do not change the electron's energy gain for the same rms size, as discussed later. The figure clearly shows that strong multipacting could occur early, just 20 ns after the bunch's center. The PSR beam is shorter than the SNS beam, and its total multipacting time is about a factor of 2 less. However, it has a bigger SEY and higher multipacting frequency due to the short transit time. Therefore, both beams have almost a similar electron cloud density. Note that the same SEY parameters are used for both beams.

Figure 11 plots the measured signal of electrons that hit the wall at LANL's PSR [33]. The number of electrons grows dramatically at the trailing edge of the proton bunch and peaks at its tail. This is consistent with the shape of the

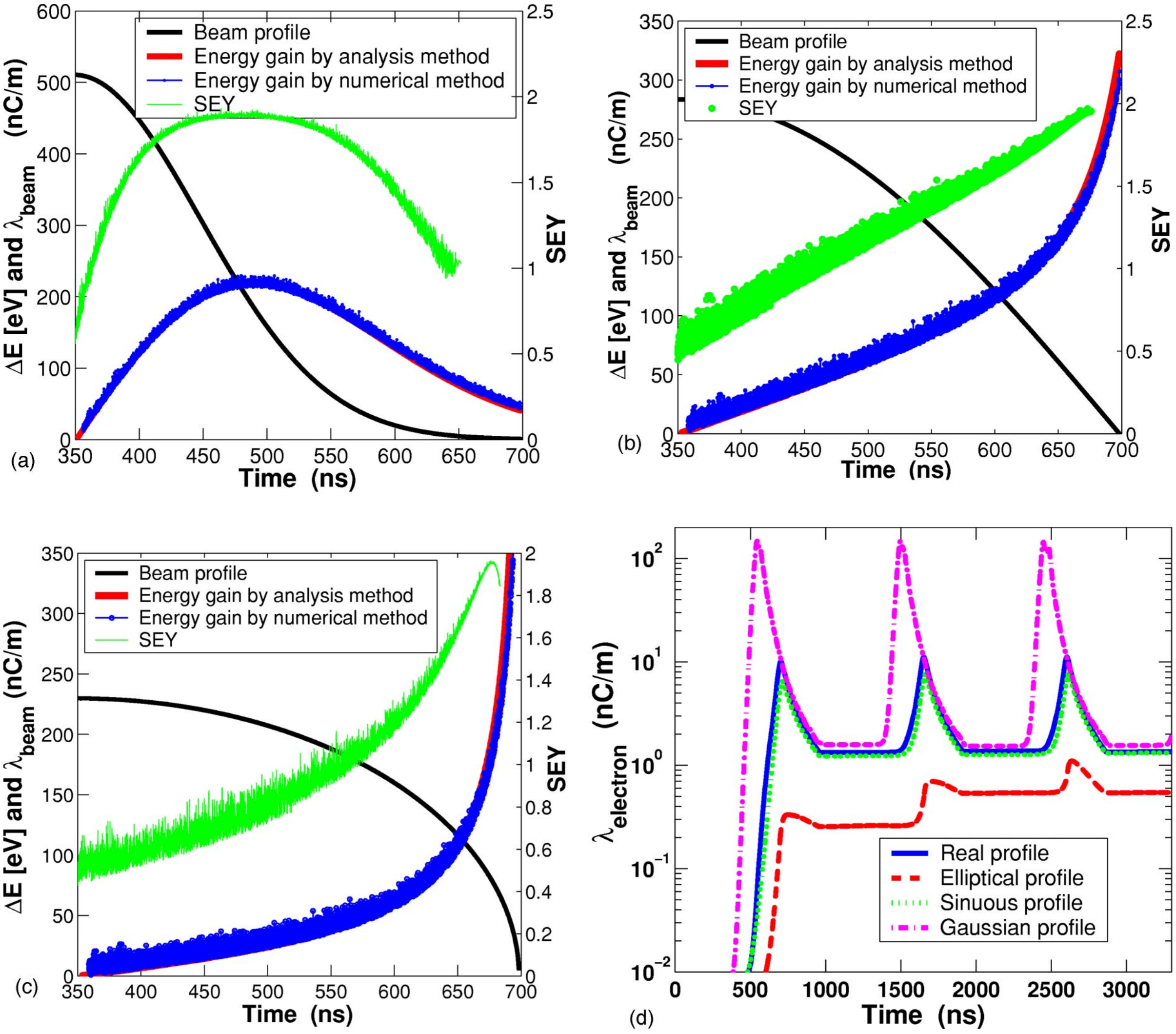

FIG. 9. (Color online) Comparison the effects of Gaussian, sinusoidal, elliptical, and realistic beam profiles for the SNS.

simulated electron wall current [Fig. 10(b)] and can be explained by the electron's energy gain [Fig. 10(a)]. The wall current due to electrons hitting it is 0.4 $\mathrm{mA/cm^2}$ experimentally [5], and is 0.6 $\mathrm{mA/cm^2}$ by simulation [Fig. 10(b)]. The measured electron energy at the wall is up to 300 eV, roughly agreeing with the simulated number 200 eV. This discrepancy may reflect differences in the experimental and simulated parameters. For example, the installation of the detector changed the geometry of the chamber and hence the energy gain.

For a given longitudinal beam profile, the electron density inside the chamber slowly changes with the bunch's length provided that the particle density inside the bunch is kept constant by maintaining the bunch's intensity proportional to its length. A long bunch reduces the electron energy gain but may increase the possible multipacting time.

If the bunch length is reduced and its intensity kept constant, the electron density inside the chamber at the bunch tail will rise quickly with a decrease in bunch length due to both a high gain in energy and a fast multipacting frequency. However, fewer electrons survive from the last bunch gap of a short bunch because of the stronger space-charge force of the electron cloud at the gap, and the long bunch gap. Simulation demonstrates that reducing the bunch's length from 700 ns to 400 ns causes a strong multipacting at its tail and low electron density inside the beam. Consequently, a short bunch may be a more stable one, depending upon the detailed parameters. The density of electrons trapped inside the beam balances the effects of multipacting and space charge. An earlier study of the PSR beam showed that a higher beam current could be stored with shorter bunch length at the same instability threshold [4]. After installing inductive inserts [34], the curves of the instability threshold are unaffected by variations in bunch length from 200 to 290 ns. This effect is unclear, as a shorter bunch length would have a smaller momentum spread (for a fixed rf voltage) and provide less Landau damping. However, a short bunch entails a long gap and less chance for electrons to survive it. Hence, these two effects would tend to cancel each other.

The beam's transverse profile and beam size

We compared the buildup of the electron cloud and the energy gain for a cylindrical beam and a Gaussian beam with

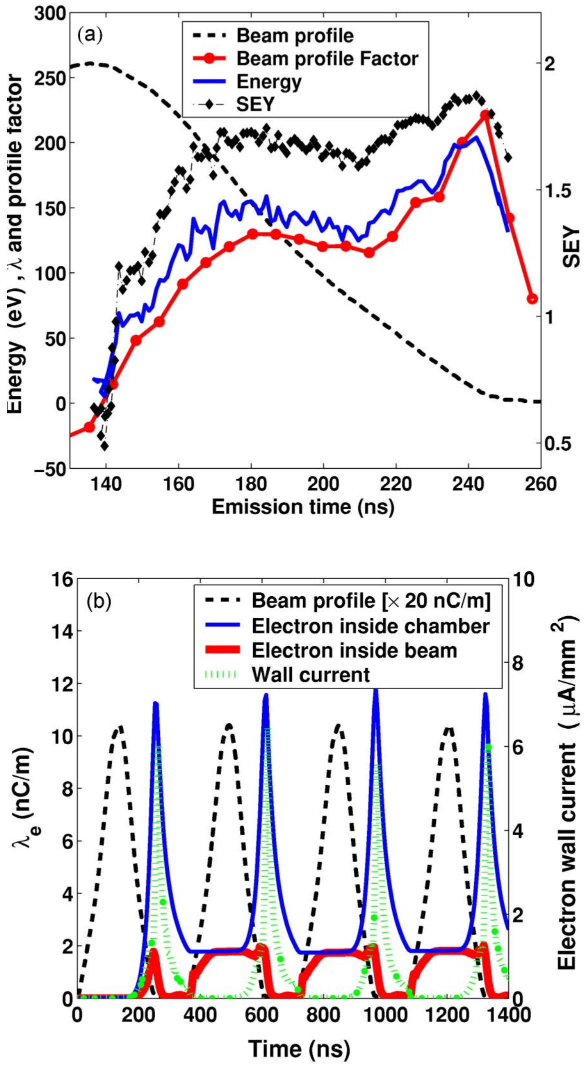

FIG. 10. (Color online) Energy gain (a) and electron-cloud buildup (b) in the PSR drift region.

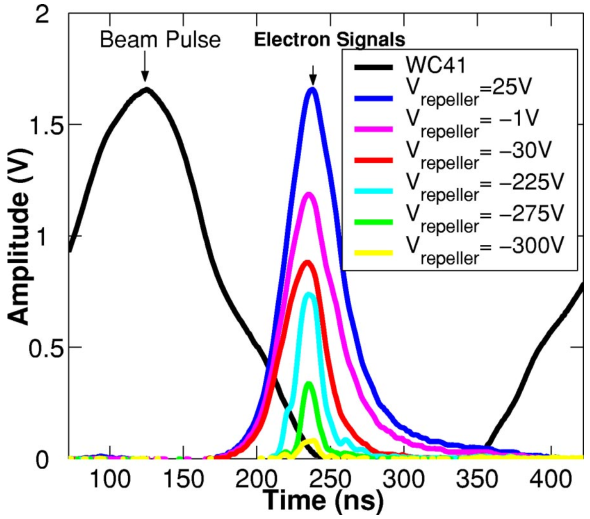

FIG. 11. (Color online) Electron signals measured at the PSR with time during a single revolution for an 8 μC/pulse beam. The repeller's voltage $V_{repller}$ is varied to select the electrons striking the detector according to their energy.

the same rms in the SNS's drift region. The two transverse profiles exhibit very similar electron densities inside the beam (the difference is less than 5%) and are equal inside the chamber. Seemingly, the space-charge force does not depend on the transverse spatial charge distribution of the beam for a given rms size [35]. This is confirmed by the electron's energy gain, which is the same for both beams. Therefore, the electron energy gain of a Gaussian beam can be estimated with the formula used for a cylindrical uniform beam with the same rms size, as given by Eqs. (15) and (16).

Although the gain in electron energy is independent of the shape of the beam's transverse profile, the azimuthal distribution of the electron cloud is related to it: the electron cloud is more expansive in the orientation of the larger beam size. Figure 12 is a simulated electron-cloud distribution in the transverse plane at different times for an assumed SNS flat beam, $\sigma_x:\sigma_y=2:1$. The space-charge force confines electrons moving along this direction at the bunch tail, where stronger multipacting then occurs. A similar phenomenon was observed in the LANL PSR [36,37].

A smaller beam size contributes to a stronger space-charge field as shown in Eq. (2), and hence larger electron energy gain and stronger multipacting. The electron energy gain roughly decreases linearly with increments of the beam's transverse size. Figure 13 shows the electron density with a different beam. The simulated electron density inside the chamber of the SNS ring is roughly inversely proportional to the transverse beam size, scaling as

$$\lambda_{chamber}(\mathrm{nC/m}) = 21 - 0.27\ a(\mathrm{mm}). \tag{18}$$

However, the electron volume density inside the beam is scaled as

$$\rho_{cen}(\mathrm{nC/cm^3}) = 4.9e^{-0.1\ a(\mathrm{mm})}. \tag{19}$$

The volume density inside the beam decreases exponentially with the beam's transverse size. Therefore, a big size is very helpful in reducing instabilities caused by the electron cloud. This is consistent with the PSR experimental study [31] wherein the instability threshold rose by a factor of 2 when the beam's size was increased from 15 mm to 34 mm.

Effects of the beam's intensity

For a fixed longitudinal beam profile shape, the energy gain calculated with Eq. (15) is proportional to the square root of the beam's intensity *N*. We used the identical number of lost protons for different beam intensities to check the latter alone; at high beam density, the density of the electron cloud increases quickly with increments in the beam's intensity, thereby predicating that the former is very sensitive to the latter. Two mechanisms explain this phenomenon. One is the energy gain; thus, a strong beam causes a larger energy gain and hence a larger SEY. The second is the higher multipacting frequency for a stronger beam. The transit time is

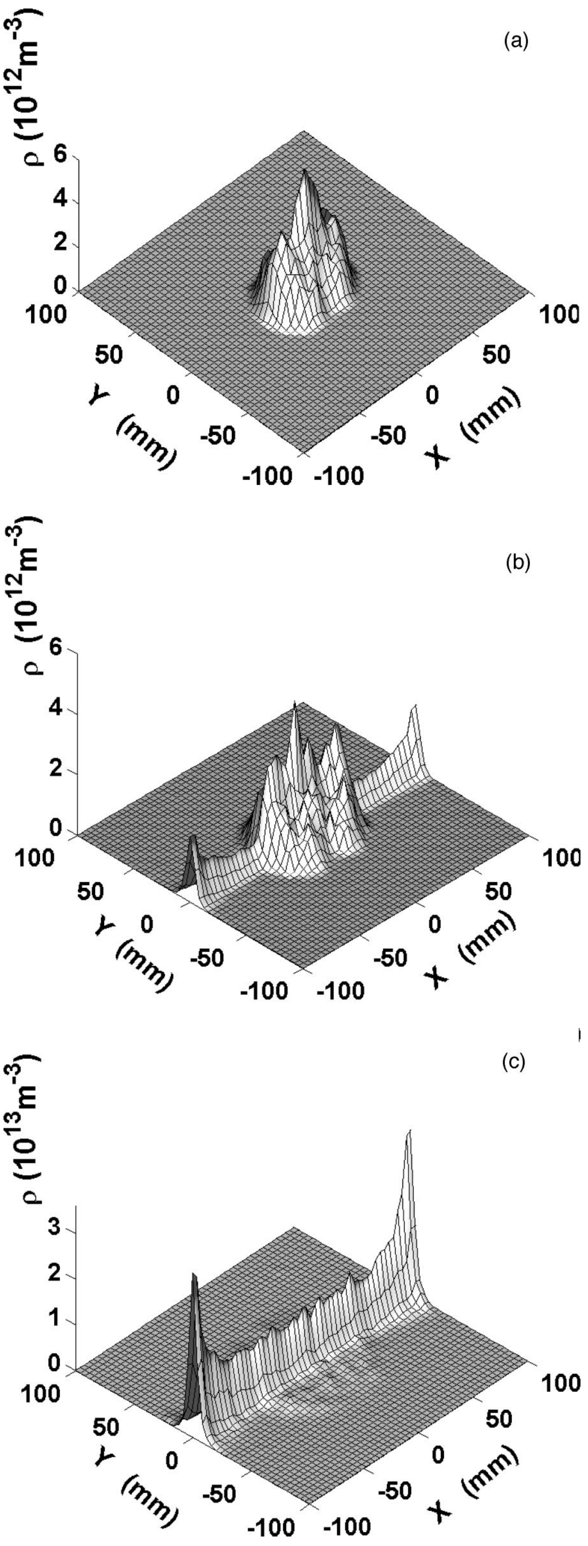

FIG. 12. Transverse distribution of electron cloud for an assumed SNS flat transverse beam profile with $\sigma_x:\sigma_y=2:1$ at 350 ns (top), 560 ns (middle), and 630 ns (bottom).

inversely proportional to $\sqrt{\lambda}$. Therefore, a more intense beam contributes to a higher multipacting frequency. By fitting the simulation result, we obtain the scaling law of electron density with beam intensity in the SNS ring as

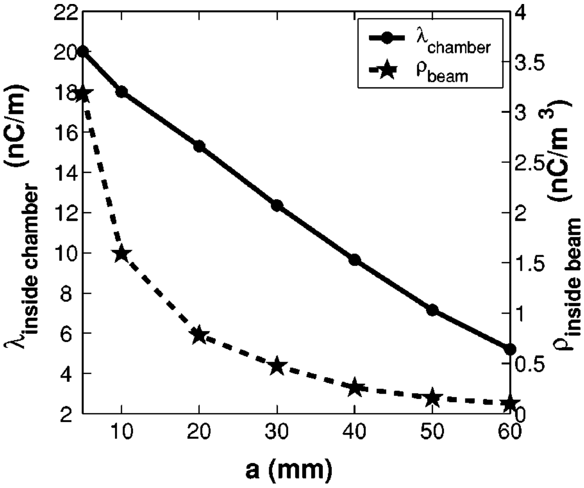

FIG. 13. The effect of transverse beam size on electron density in the SNS drift region.

$$\lambda_{chamber}(\mathrm{nC/m}) = (78-112)\times 1.0^{-14}N + 39\times 1.0^{-28}N^2. \quad (20)$$

The combined effects of multipacting frequency, energy gain, and space-charge force increases electron density as the beam's intensity rises. In the PSR, the measured electron-cloud signal shows a similar strong dependence on beam intensity [5].

On the other hand, the density of the electron cloud inside the beam may become saturated, or even decrease at high beam intensities (Fig. 14). With an increase in bunch intensity, the number of electrons inside the chamber during the bunch gap also rises, and hence the space-charge field. The stronger space-charge force entails a short decay time for the electron cloud during the gap. As a result, a high beam intensity affects the number of electrons inside the chamber in two ways: increasing it by stronger multipacting, and reducing it by promoting a quicker decay at the bunch gap. We note that the number of electrons inside the beam roughly equals the number surviving from the last bunch gap due to

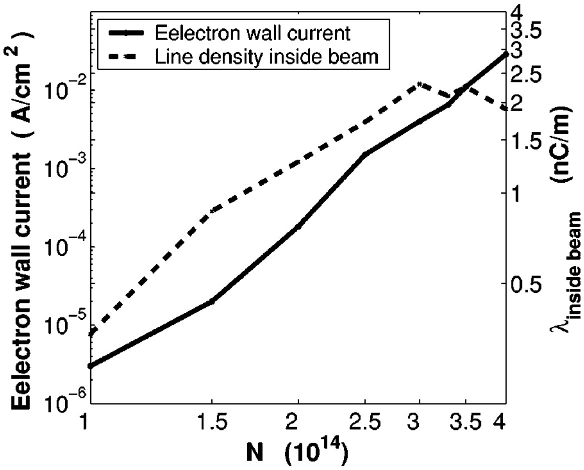

FIG. 14. Electron wall current and average line density inside the beam in the SNS drift region.

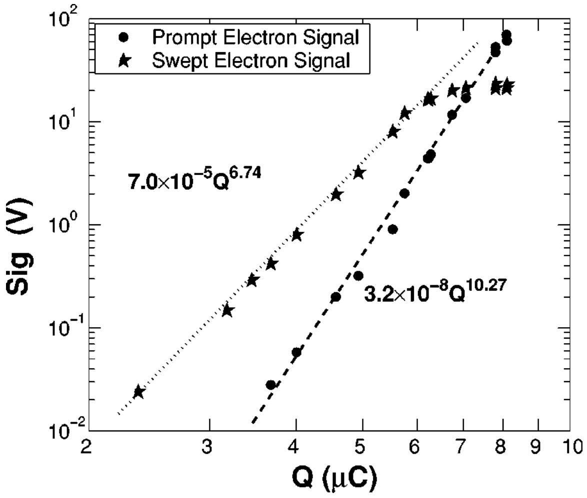

FIG. 15. Measured prompt electron and swept electron signal amplitudes plotted against the stored beam intensity in LANL's PSR. All other beam parameters were fixed, including the buncher voltage and accumulation time.

the beam's trapping effect (Figs. 4 and 6). This mechanism can explain the saturation or decrease of electron density inside the beam when multipacting is very strong.

We measured the electron signal, the so-called prompt electron signal, in the PSR when the electrons strike the chamber wall, which corresponds to the simulated wall current in Fig. 14. An electron-sweeping detector was used to measure electrons lingering inside the pipe [38]. Basically, it is a retarding field analyzing detector (RFA) with an electrode opposite the RFA. The electrode is pulsed with a short fast pulse (up to 1 kV) to sweep low-energy electrons at the bunch gap from the pipe into the detector. These "swept" electrons correspond to the simulated surviving electrons from the bunch gap. Figure 15 shows the measured prompt electron signal and swept electron signal with different bunch intensities in the PSR [39]. While the prompt electron signal increases without saturation, the swept electron signal saturates at high beam intensity. These experimental results qualitatively agree with the simulation of the SNS (Fig. 14). In the PSR experiments the instability threshold curves are linear up to the maximum intensity we achieved, i.e., 10 μC/pulse. According to the physics model, beam instabilities are sensitive to the electrons inside the beam and hence the instability threshold should saturate at this high intensity. We cannot explain the discrepancy between the measured electron cloud density and the threshold for beam instability.

Bunch gap

The effects of the trapped electrons surviving from the last bunch gap play a major role in the operation of the long bunch because electrons inside the beam are the main source of electron-proton instabilities [32]. Although strong multipacting occurs at the bunch's tail, most electrons remain outside the beam (Fig. 7). The electrons' density inside the beam at the tail is at the same level as at other times, as shown in Figs. 6 and 10. Therefore, surviving electrons from the last bunch gap cause instabilities.

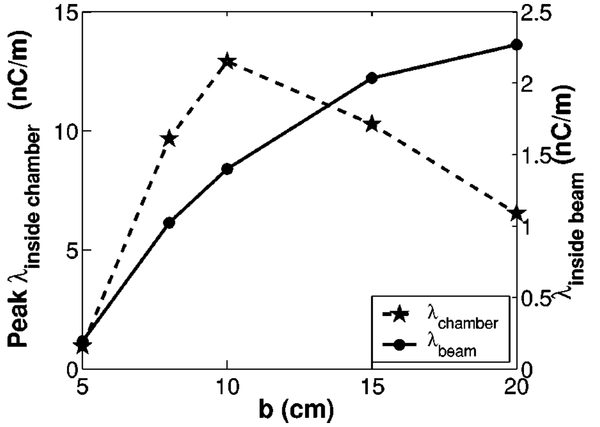

FIG. 16. Electron density as a function of chamber size with constant beam size.

We note that the bunch gap has a very weak effect on the peak electron line density inside the chamber due to the single-bunch multipacting mechanism. Therefore, this peak density is almost the same during the passage of the first turn and of the following ones (Figs. 6 and 10). However, the bunch gap contributes to reducing the electron density inside the beam. If the gap is longer than the decay time of the electron cloud, the electron density inside the beam will be lowered significantly, and hence the beam's instabilities also. When the bunch gap is short such that the electron cloud cannot decay to zero by its end, a clearing electrode can be applied to remove the electron cloud. A weak clearing field can clear electrons at the bunch gap and significantly lower the number of electrons inside the beam during the bunch's passage.

The protons remaining at the bunch gap, due to their wider momentum spread and large pulse width, can slow down electron loss because of the space-charge effect. The percentage of protons at the gap is less than 1×10^{-4} for the SNS design beam. The simulated electron line density inside the chamber increases by 18% and 33%, respectively, for 1×10^{-4} and 1×10^{-2} protons at the gap. However, the electron density inside the beam increases by 30% and 300%, respectively, because they decay slowly during the gap. Since the growth rate of the beam's instability is proportional to the electron density inside the beam, instability should be highly sensitive to the beam at the gap, even though that parameter itself has a weak effect on the average electron density inside the chamber. The PSR experiment shows that the number of trapped electrons is a factor of 3 higher with a 1% beam in the gap [37], which is close to the simulation result for the SNS ring.

Effects of chamber size

The energy gain in Eq. (15) is almost a linear function of the vacuum chamber's size b. A large chamber imposes a long transit time, and hence larger gains in energy. The SEY is very different for $b=5$ cm and 10 cm; however, the difference decreases when b increases further because the SEY

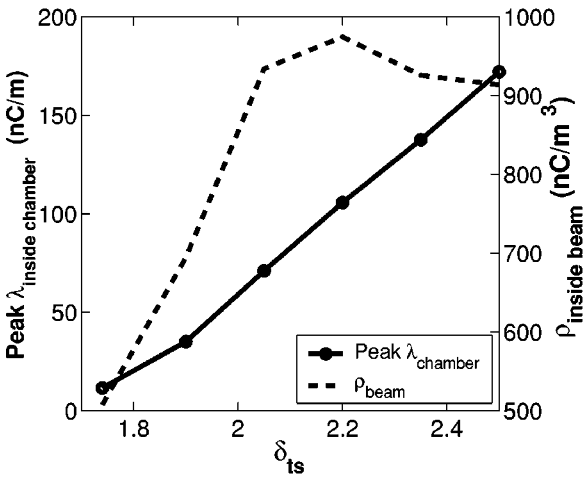

FIG. 17. The effects of peak SEY on electron density in the SNS ring.

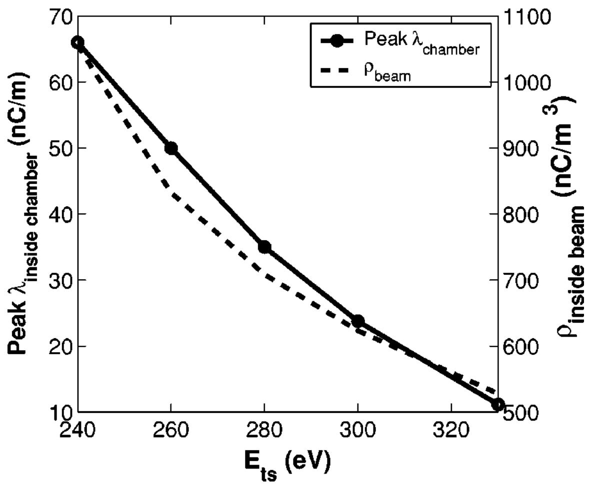

FIG. 18. The effects of energy at peak SEY on electron density in the SNS ring.

varies slowly when the incident energy is closer to the energy at peak SEY (Fig. 1). It is interesting that the electron density inside the chamber rises with b and then falls if b increases further. Two rules govern the character of the electron density with b. A larger b contributes to higher energy and hence a larger SEY up to the point where the electron energy reaches the peak of the SEY curve. However, the electron transit time also is longer for a larger b. Consequently, a larger b gives a larger SEY and lower multipacting frequency. Note that, while SEY is not sensitive to b when b is large enough, the multipacting frequency is. Therefore, the electron density has a maximum value for the median b. For the SNS, this value is 10 cm, exactly the radius of the SNS's design chamber. However, electron density inside the beam increases with the size of b and saturates at around 15 cm, as shown in Fig. 16.

In a real machine, the beam's chamber is big when its local beam is large. In general, the ratio of beam chamber size to that of the beam is roughly constant along the storage ring. Therefore, both vary along the ring. Keeping the ratio of b to a constant, the electron-cloud line density inside the chamber peaks at the median of b. However, the volume density inside the beam decreases linearly with increasing b. Therefore, employing a large-sized beam and chamber can reduce the beam's instabilities.

Peak SEY and energy at peak SEY

The density of the electron cloud is very sensitive to peak SEY when multipacting occurs due to its exponential growth. In the absence of a space-charge effect, the electron density should increase exponentially with SEY. Figure 17 shows the electron line density for different peak SEYs. Electron density inside the chamber increases linearly with peak SEY, at a rate slower than exponential growth due to the effect of the space charge. In contrast, the average volume electron density inside the beam approaches saturation for a big peak SEY due to the strong space-charge effect. Because beam instability is governed primarily by the volume density inside the beam, we conclude that the beam's instabilities will saturate at a certain peak SEY. However, the heat load in the SNS ring caused by the electron cloud hitting the chamber does not saturate until the peak SEY is 2.5.

The electron energy gain with a long beam, which usually is less than the energy at the peak SEY, is much smaller than that with a short bunch, such as in B factories where the gain in energy can be high, up to a few keV. Accordingly, a long beam is more sensitive to the energy at peak SEY which has equivalent effects as the peak SEY. Figure 18 shows the electron density for different energies at peak SEY. Both the electron line density inside the chamber and the electron volume density inside the beam increase linearly with the decrement of energy at peak SEY. The latter does not reach saturation because the former is not large enough. If the energy at peak SEY falls from 330 eV to 246 eV, the electron density inside the chamber will increase from 12 nC/m to 67 nC/m. The effect is the same as increasing the SEY from 1.74 to 2.07. However, the effect on electron density inside

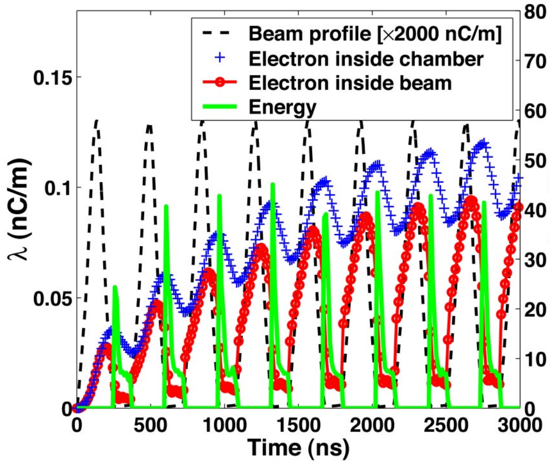

FIG. 19. (Color online) Simulated electron-cloud buildup due to ionization in the PSR's drift region. We reduced the beam's profile by a factor of 2000 to clearly display it, together with electron-cloud density. The electron average energy on hitting the chamber surface is also shown.

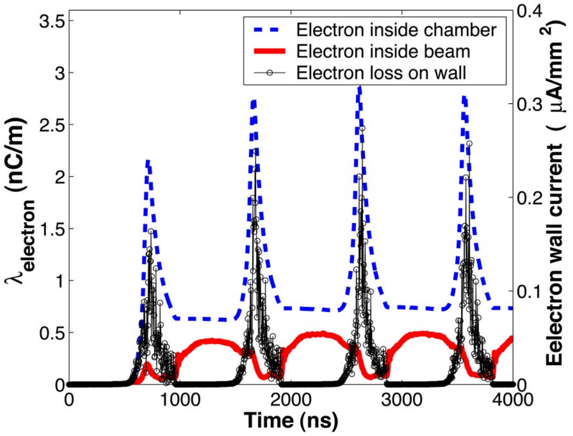

FIG. 20. (Color online) Electron-cloud buildup in the SNS dipole.

the beam is stronger than increasing the SEY from 1.74 to 2.5. Therefore, a bigger energy at peak SEY can significantly reduce the beam's instability.

Electron by ionization

The number of electrons generated by the residual gas depends on its pressure and temperature. The yield usually is more than one order of magnitude less than the yield of electrons by proton loss when the vacuum is good, depending upon machine design. These electrons, with low initial energy [40], are trapped deep inside the beam during the beam's passage and released at the bunch's tail. According to Eqs. (4) and (10), the possible maximum energy gain when an electron is released at the end of the bunch is 130 eV for the SNS beam. An electron generated by ionization can hit the chamber surfaces only a few of times, typically twice for the SNS beam, at a bunch gap with low energy. Therefore, they cannot excite multipacting.

Figure 19 shows the simulated buildup of the electron cloud for the PSR beam assuming that electrons are initially generated by ionization at 70 nTorr pressure with a yield the same as from proton loss (Table I). Note that there is no multipacting for either the SNS or PSR beam because the energy of the electrons is low when they hit the chamber wall; i.e., under 120 eV for the SNS and 60 eV for the PSR. This agrees with our estimation. The electron cloud accumulates during the beam's passage due to its trapping effect by the beam and decays slowly at the bunch gap. When these two processes are balanced, the electron cloud saturates.

Although the electron-cloud density from ionization is negligible compared with that due to electrons generated by proton loss for both the SNS and PSR provided their vacuum pressure is satisfactory, when it is poor, notable numbers will be generated by ionization, and all can be trapped inside the beam and destabilize it without strong multipacting, as in CERN's ISR where the beam is coasting [2,3]. The electron cloud's density in LANL's PSR is roughly proportional to the chamber's vacuum pressure when the vacuum is poor [41].

Dipole magnetic field and other fields

In dipole magnets, only electrons moving near the center of the horizontal chamber have enough energy at the wall's surface to form a multipacting cloud as described by Eq. (16) and shown in Fig. 8. Figure 20 shows the electron-cloud buildup in the SNS's dipole magnet. Its pattern is similar to that in the drift region because, in both, the energy gain has the same dependence on the beam's line density. The electron cloud is about twice as small as that in the drift region due to the limitation of the multipacting area in the dipole magnet. The simulated distribution of the electron cloud in a dipole magnet (Fig. 21) is consistent with the gain in electron energy (Fig. 8). The electron cloud is trapped vertically by the beam's space-charge force at the chamber's center during the beam's passage. As in the drift region, there is strong multipacting at the tail. In the present proton machine, multipacting can occur only at the chamber's horizontal center because the electron energy peaks there below a few hundreds of eV. It is less than 300 eV in the SNS dipole magnet. However, in short-bunch machines, for example the SPS and B factories, the energy of an electron hitting the wall's surface at the horizontal center of the chamber could be more than thousands of eV under normal operational parameters,

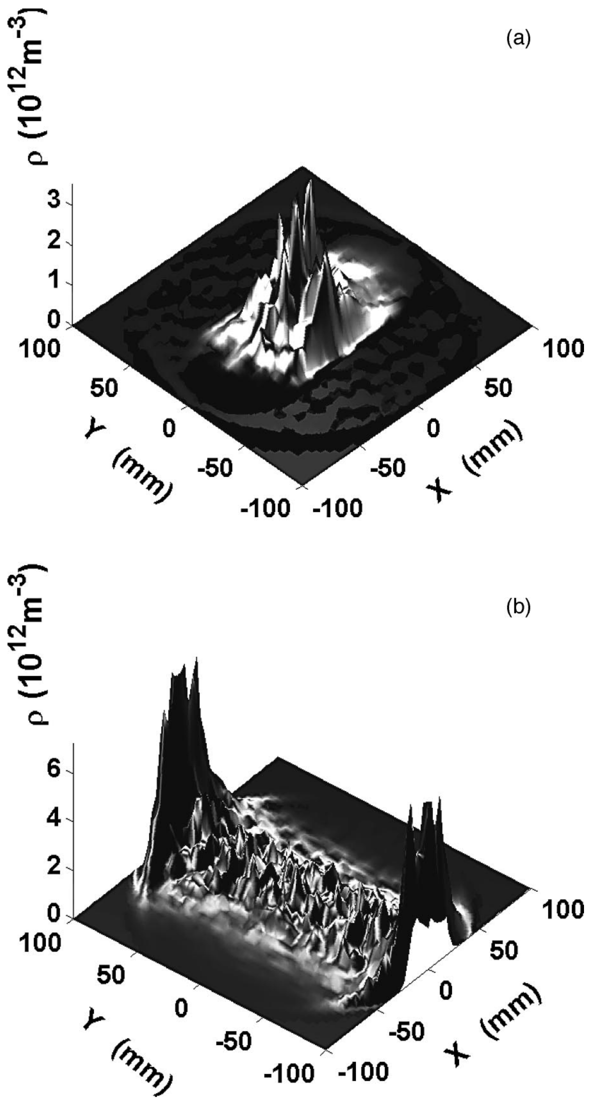

FIG. 21. Electron transverse distribution in the SNS dipole magnet at bunch's center (top) and tail (bottom).

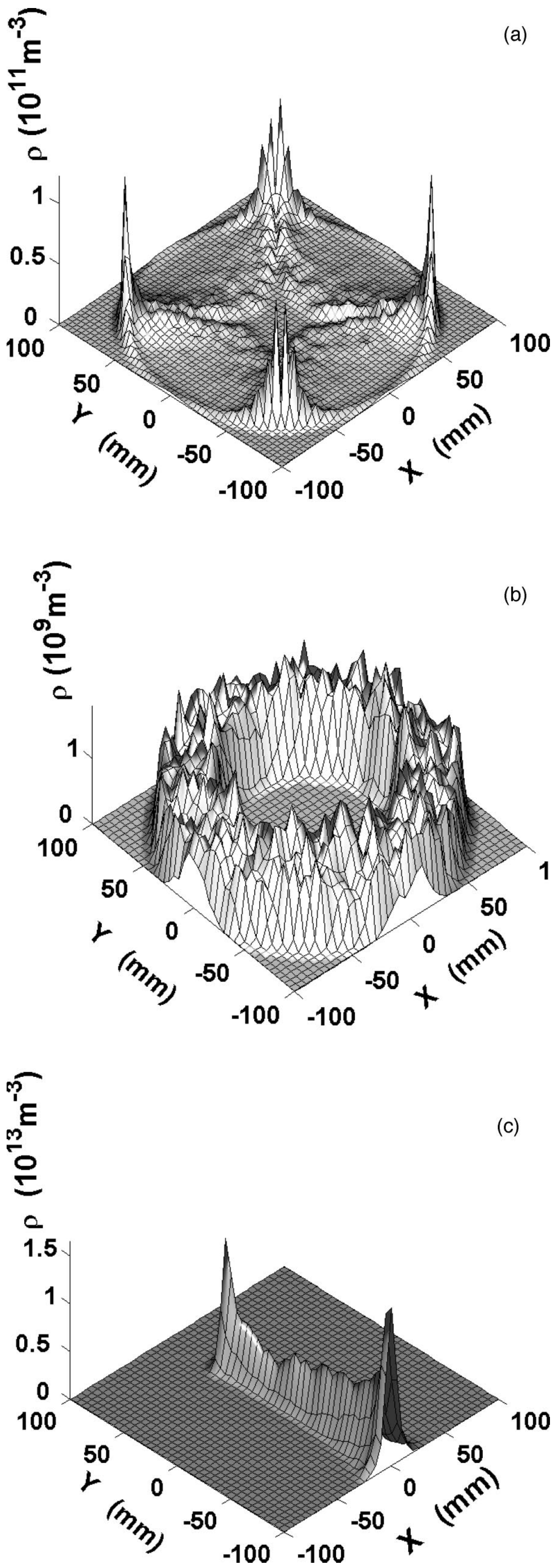

FIG. 22. Electron transverse distributions in the SNS's quadrupole with a field gradient of 4.7 T/m (a); 30 G solenoid magnets (b); and the clearing electrode with 2 kV clearing voltage (c).

inducing multipacting at two strips near the center [12,19].

Figure 22 shows the results of simulations for the electron cloud's transverse distributions in a normal quadrupole magnet, a solenoid, and the electric clearing electrode of the SNS ring. In quadrupole magnets, very weak multipacting occurs around the middle of each magnetic pole at the bunch tail because only those electrons moving along these field lines receive enough energy by a mechanism similar to that inside a dipole magnet. The simulated electron cloud is more than two orders of magnitude smaller than in the drift region due to the electron's low energy at the wall's surface. Quadrupole and sextuple magnet fields are mirror fields that may trap electrons via the mirror-field trap mechanism. However, mirror-field trapping requires that the bunch length is shorter than the period of gyration [42]. Therefore, electrons emitted from the chamber's surface cannot be trapped due to the long bunch length. The distribution of the electron cloud shown in Fig. 22 implies that there is no mirror-field trap; the electron cloud would stay closer to the mirror points of the field lines if mirror-field trapping happened. Compared with the electron cloud in the drifting region, the simulated decay time of the electron cloud at the bunch gap in quadrupole and sextupole magnets is much longer due to the weak space-charge effect, and the confinement of the electron's orbit by the magnetic fields. As in the drift region and dipole magnet, the electron cloud is trapped by the beam's space-charge force at the chamber's center during the passage of the beam center.

A 30 G weak solenoid can be invaluable in confining the electron cloud to the region near the wall and limiting the energy of electrons hitting the wall's surface to below the multipacting level. Electron density inside the chamber can be lowered a thousandfold. There is a nonelectron circle region at the chamber's center with a radius greater than the transverse beam size. Macek's PSR experiment demonstrated that a 20 G solenoid field reduces the electron signal by a factor of 50 [30]. We note that the solenoid field in that experiment was nonuniform, which has a weaker effect than a uniform one [43].

The effect of a clearing electrode is more complicated because it disturbs the electron's orbit and energy gain. A weak voltage round 200 V can effectively suppress multipacting. On the other hand, a median clearing voltage, which is 2000 V in the SNS, can excite stronger multipacting than can zero clearing fields. We suggested how electron motion under a clearing field could explain the field's mechanism of action [43].

CONCLUSIONS

We studied in detail electron motion under a beam's space-charge field. The adiabatic invariant clearly describes the oscillatory amplitude of the trapped electrons. Combining these data with the longitudinal beam profile, we gained information about the trapped electrons, such as loss time and location. The electrons surviving from the last bunch gap destabilize the proton beam because huge numbers of them are trapped deep inside the beam during its passage. However, these surviving electrons have a weak effect on multipacting due to their protracted trapping and low energy at the wall. On the other hand, electrons created at the wall can excite electron multipacting at the bunch's tail. Our estimation of the gain in the multipacting electron's energy when it hits the chamber wall is consistent with the numerical result. Further, its energy gain clearly shows how and when multipacting occurs. According to the longitudinal beam profile factor, the gain in electron energy is usually bigger around the tail of the bunch; consequently, multipacting is stronger there. Our analysis quantitatively explains the mechanism of the "trailing-edge multipactor."

Various factors related to the electron multipacting were investigated; the beam's longitudinal and transverse profiles, its intensity, the chamber size, the bunch gap, and the SEY. Among them, multipacting is most sensitive to the beam intensity. The electron density grows quickly with increases in the beam intensity due to the combined effects of multipacting frequency and energy gain.

The longitudinal profile of the beam also plays a very important role in multipacting at the trailing edge. The longitudinal beam profile factor [Eq. (17)] can be used to directly estimate the beam profile's effect. According to our study, the bunch tail usually contributes to strong multipacting when this is large, explaining why cutting the tail can effectively reduce multipacting. Thus, we can optimize the design of a real machine to reduce the beam profile factor. The energy spreader and corrector can significantly suppress the beam's tail [44], hence reducing multipacting. There is no multipacting for a coasting beam due to the zero longitudinal beam profile factor.

By contrast, the transverse beam profile has weak effects on electron multipacting. A Gaussian beam and a uniform cylindrical beam of the same rms size exhibit the same electron energy gain and electron-cloud buildup. A beam with smaller transverse size contributes to stronger multipacting. The electron line density inside the chamber decreases linearly with the transverse beam size while the electron volume density inside the beam decreases exponentially. Therefore, beam instability is more sensitive to transverse beam size, and a larger one can weaken the electron-proton instabilities. On the other hand, the beam's azimuthal distribution significantly affects the multipacting. For a flat beam, stronger multipacting occurs in the orientation of larger beam size.

The bunch gap is important when the electron-cloud decay time is longer than the gap. Where the gap is not long enough to clear the electron cloud, an electric clearing field can effectively do so. The electron cloud surviving from the bunch gap between subsequent bunches, and hence the beam's instability, is also sensitive to the beam in the gap. Multistage beam cleaning that includes multistep chopping at low energies and beam-in-gap sweeping with collimator collection at the top energy ensures a clean gap.

The secondary emission parameters directly affect electron multipacting. The electron cloud within the chamber increases roughly linearly with the increase of peak SEY in the SNS ring. However, the electron cloud within the beam saturates at high SEY due to the strong space-charge force at the bunch gap. Except for the peak SEY, energy at the peak SEY also has a very important effect on a long bunch because the maximum gain in energy is close to the energy at the peak SEY. Increasing the latter can significantly reduce multipacting and electron-proton instabilities.

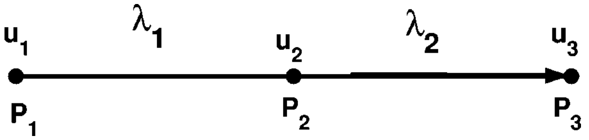

FIG. 23. Scheme of electron energy gain.

The size of the chamber has both advantages and disadvantages for electron multipacting. Larger chambers entail a larger electron energy gain and lower multipacting frequency.

Electrons generated by ionization have a weak effect on multipacting because they are trapped inside the beam during its passage. However, when the vacuum is poor, these trapped electrons can excite strong electron-proton instabilities without multipacting.

Multipacting occurs at the horizontal chamber's center in a dipole magnet due to the high energy gain there. The electron density in dipole magnet is reduced to one-third of the electron density in the drift region due to the limitation of the multipacting area in the dipole magnet. There is weak multipacting in quadrupole and sextuple magnets where the electron density is two orders of magnitude lower than in the drift region. There is no mirror-field trapping in the quadrupole magnet due to the long bunch length. A weak solenoid field up to 30 G can confine all electrons near the wall surface and reduce the electron density by a factor of one thousand in the drift region.

ACKNOWLEDGMENTS

We gratefully thank Professor A. Chao, Dr. A. Browman, Dr. A. Fedotov, Dr. P. He, Dr. H. Hseuh, Dr. Y. Y. Lee, Dr. D. Raparia, Dr. T. S. Wang, Dr. S. Y. Zhang, and Dr. F. Zimmermann for many useful discussions. This work was performed under the auspices of the U.S. Department of Energy. The Spallation Neutron Source is managed by UT Battelle, LLC, under Contract No. DE-AC05-00OR22725 for the U.S. Department of Energy. SNS is a partnership of six national laboratories: Argonne, Brookhaven, Jefferson, Lawrence Berkeley, Los Alamos, and Oak Ridge.

APPENDIX A: ENERGY GAIN OF MULTIPACTING ELECTRON IN DRIFT REGION

One multipacting electron emitted from the chamber surface will move straight to the opposite wall surface. The potential given by Eq. (4) varies during the beam's passage due to the variation of its line density. For convenience, we assume the following linear dependence:

$$U(r,t) = \lambda(t)u(r). \tag{A1}$$

Figure 23 schematically plots the motion of an electron for a short interval. One electron moves from point P_1 to P_2 with beam line density λ_1 and then moves to P_3 with beam line density λ_2. During the movement from P_1 to P_3, the change of electron kinetic energy is

$$\Delta E = -e\Delta U = -e\lambda_2(u_3 - u_2) - e\lambda_1(u_2 - u_1). \qquad \text{(A2)}$$

Rewriting Eq. (A2), we get

$$\begin{aligned} \Delta E &= e(\lambda_1 u_1 - \lambda_2 u_3) + eu_2(\lambda_2 - \lambda_1) \\ &= e(\lambda_1 u_1 - \lambda_2 u_3) + eu_2\Delta\lambda \\ &= \Delta E_1 + \Delta E_2. \end{aligned} \qquad \text{(A3)}$$

The first part of the energy gain when the electron hits the wall is

$$\Delta E_1 = -eu(b)\Delta\lambda = -\frac{e\Delta\lambda}{4\pi\varepsilon_0}\left(1 + 2\ \ln\frac{b}{a}\right) \qquad \text{(A4)}$$

where b is the radius of the vacuum chamber and $\Delta\lambda$is the difference in bunch density between the moments of emission and of loss. Note that $\Delta\lambda < 0$ for a multipacting electron. Assuming that the beam line density is a linear function of time during the electron's short transit time, $\Delta\lambda$ can be written as

$$\Delta\lambda \approx \frac{\partial\lambda}{\partial t}\Delta t = \frac{\partial\lambda}{\partial z}c\beta\Delta t, \qquad \text{(A5)}$$

where Δt is the transit time. The transit time can be estimated as the half period of the oscillation with amplitude b:

$$\Delta t = \frac{1}{2}T(b) = 2.0\sqrt{\frac{\pi\varepsilon_0 m}{\lambda e}}\left(\sqrt{2}a\ \arcsin\frac{1}{\sqrt{1 + 2\ \ln(b/a)}} + \int_a^b \frac{dr}{\sqrt{\ln(b/r)}}\right). \qquad \text{(A6)}$$

Combining Eqs. (A4)–(A6), the first part of the energy gain is

$$\Delta E_1 \approx -\beta c\sqrt{\frac{me}{4\pi\varepsilon_0}}\left(\sqrt{2}a\ \arcsin\frac{1}{\sqrt{1 + 2\ \ln(b/a)}} + \int_a^b \frac{dr}{\sqrt{\ln(b/r)}}\right)\left(1 + 2\ \ln\frac{b}{a}\right)\frac{\partial\lambda}{\partial z}\frac{1}{\sqrt{\lambda}}. \qquad \text{(A7)}$$

The secondary part of the energy gain in Eq. (A3) becomes

$$\Delta E_2 = e\sum_i u_{2i}\Delta\lambda_i \approx \frac{e}{2}\int u\frac{\partial\lambda}{\partial t}dt = \frac{e}{2}\frac{\partial\lambda}{\partial t}\int udt. \qquad \text{(A8)}$$

The electron quickly drifts from one side of the chamber wall to another. By integrating throughout the whole traversal, the above equation can be written as

$$\Delta E_2 = \frac{1}{2}\beta c\sqrt{\frac{me}{2\pi\varepsilon_0}}\left[a\left(\arcsin\frac{1}{\sqrt{1 + 2\ \ln(b/a)}} - \sqrt{2\ \ln\frac{b}{a}}\right) + \frac{1}{\sqrt{2}}\int_a^b \frac{1 + 2\ \ln(r/a)}{\sqrt{\ln(b/r)}}dr\right]\frac{\partial\lambda}{\partial z}\frac{1}{\sqrt{\lambda}}. \qquad \text{(A9)}$$

From Eqs. (A7) and (A9), we obtain the total energy gain when one electron hits the wall surface as

$$\Delta E = -\frac{1}{2}\sqrt{\frac{me}{2\pi\varepsilon_0}}\beta c\left(a(2\zeta - 1)\arcsin\frac{1}{\sqrt{\zeta}} + a\sqrt{2\ \ln\frac{b}{a}} + \sqrt{2}\zeta\int_a^b \frac{dr}{\sqrt{\ln(b/r)}} - \frac{1}{\sqrt{2}}\int_a^b \frac{1 + 2\ \ln(r/a)}{\sqrt{\ln(b/r)}}dr\right)\frac{\partial\lambda}{\partial z}\frac{1}{\sqrt{\lambda}} \qquad \text{(A10)}$$

with $\zeta = 1 + 2\ \ln(b/a)$.

APPENDIX B: ENERGY GAIN OF MULTIPACTING ELECTRON IN DIPOLE MAGNET

The equation of motion of a charged particle in electric and magnetic fields is

$$m\frac{d\boldsymbol{v}}{dt} = e\mathbf{E} + e\boldsymbol{v} \times \mathbf{B}. \qquad \text{(B1)}$$

In dipole magnets, $\mathbf{B} = (0, B_y, 0)$ and the beam's electric field $\mathbf{E} = (E_x, E_y, 0)$. The longitudinal beam field is small, and is neglected here. The equation of motion then becomes

$$\frac{d\upsilon_x}{dt} = \omega\upsilon_z + \omega E_x/B, \qquad \text{(B2)}$$

$$\frac{d\upsilon_y}{dt} = eE_y/m, \qquad \text{(B3)}$$

$$\frac{d\upsilon_z}{dt} = -\omega\upsilon_x, \qquad \text{(B4)}$$

where $\omega = eB/m$is the gyration frequency in the magnet. Substituting υx from Eq. (B4) into Eq. (B2),

$$\frac{d^2\upsilon_z}{dt^2} + \omega^2\upsilon_z = -\omega E_x/B. \qquad \text{(B5)}$$

The initial conditions are given at $t = 0$ where $\upsilon_x(0) = \upsilon_{x0}$, $E_x(0) = E_{x0}$, and $\upsilon_z(0) = \upsilon_{z0}$. With the applied initial condition, the result becomes

$$\upsilon_x = \upsilon_{x0}\cos\omega t + \upsilon_{z0}\sin\omega t + \frac{\omega}{B}\sin\omega t\int_0^t E_x\sin\omega t dt + \frac{\omega}{B}\cos\omega t\int_0^t E_x\cos\omega t dt, \qquad \text{(B6)}$$

$$\upsilon_z = \upsilon_{z0}\cos\omega t - \upsilon_{x0}\sin\omega t + \frac{\omega}{B}\cos\omega t\int_0^t E_x\sin\omega t dt - \frac{\omega}{B}\sin\omega t\int_0^t E_x\cos\omega t dt. \qquad \text{(B7)}$$

We further integrate the expressions for υ_x and υ_z partially once and twice, respectively [45],

$$v_x = v_{x0}\cos\omega t + \left(v_{z0} + \frac{E_{x0}}{B}\right)\sin\omega t + \frac{1}{\omega B}\left(\dot{E}_x - \dot{E}_{x0}\cos\omega t - \cos\omega t\int_0^t \ddot{E}_x\cos\omega t dt - \sin\omega t\int_0^t \ddot{E}_x \sin\omega t dt\right), \tag{B8}$$

$$v_z = \left(v_{z0} + \frac{E_{x0}}{B}\right)\cos\omega t - v_{x0}\sin\omega t - \frac{1}{B}\left(E_x + \cos\omega t\int_0^t \dot{E}_x\cos\omega t dt - \sin\omega t\int_0^t \dot{E}_x\sin\omega t dt\right). \tag{B9}$$

The overdot on E represents the derivative with respect to time t.

When the beam's space-charge field changes slowly compared with the gyration frequency, i.e., when

$$\left|\frac{\dot{E}_x}{\omega E_x}\right| \ll 1, \tag{B10}$$

the integrals in Eqs. (B8) and (B9) become very small and can be neglected. In the normal dipole magnet of the SNS ring, the gyration frequency is about 20 GHz with small gyration radius less than 0.01 mm where Eq. (B10) is satisfied. Using the substitutions

$$v_z' = v_z + \frac{E_{x0}}{B}, \tag{B11}$$

$$v_{z0}' = v_{z0} + \frac{E_{x0}}{B}, \tag{B12}$$

we find that the motion in the present approximation will consist of a gyration with velocity v' superimposed on a translation with drift velocity $\mathbf{E}\times\mathbf{B}/B^2$ that varies slowly with time. The kinetic energy of gyration depends on the initial condition when the electron is created, which is around a few eV. The cross-field drifting energy at the wall's surface of the dipole magnet is less than 10 eV in the SNS, where the peak beam electric field is about 10 kV/m and the magnetic field is 0.8 T. As shown in Eq. (B3), vertical motion is independent of horizontal and longitudinal motion. An electron may receive energy from the beam due to the beam's vertical space-charge field. Following the same procedure as in the drift region, we assess the energy gain in a dipole magnet for an electron moving along the vertical magnetic field line located at horizontal coordinate X as

$$\Delta E = -\frac{1}{2}c\beta\sqrt{\frac{me}{2\pi\varepsilon_0}}\frac{\partial\lambda}{\partial z}\frac{1}{\sqrt{\lambda}}(\mathcal{T}_1 + \mathcal{T}_2 + \mathcal{T}_3) \quad (|X| < a), \tag{B13}$$

$$\Delta E = -\frac{1}{2}c\beta\sqrt{\frac{me}{2\pi\varepsilon_0}}\frac{\partial\lambda}{\partial z}\frac{1}{\sqrt{\lambda}}\int_0^{\sqrt{b^2-X^2}}\frac{2b^2 - X^2 - y^2}{X^2}\left(\ln\frac{b^2}{X^2+y^2}\right)^{-1/2}dy \quad (|X| > a) \tag{B14}$$

with

$$\mathcal{T}_1 = 2\left(1 - \frac{X^2}{a^2} + \ln\frac{b^2}{a^2}\right)\left(aG + \int_{\sqrt{a^2-X^2}}^{\sqrt{b^2-X^2}}\left(\ln\frac{b^2}{X^2+y^2}\right)^{-1/2}dy\right), \tag{B15}$$

$$\mathcal{T}_2 = -\int_0^{\sqrt{a^2-X^2}}\frac{y^2}{a^2}\left[\ln\left(1 - \frac{X^2-y^2}{\mathrm{a}^2} + \ln\frac{b^2}{a^2}\right)\right]^{-1/2}dy, \tag{B16}$$

$$\mathcal{T}_3 = -\int_{\sqrt{a^2-X^2}}^{\sqrt{b^2-X^2}}\left(1 - \frac{X^2}{a^2} + \ln\frac{X^2+y^2}{a^2}\right)\left[\ln\left(\frac{b^2}{X^2+y^2}\right)\right]^{-1/2}dy, \tag{B17}$$

$$G = \arcsin\left[\frac{\sqrt{a^2-X^2}}{a}\left(1 - \frac{X^2}{a^2} + \ln\frac{b^2}{X^2+a^2}\right)^{-1/2}\right]. \tag{B18}$$

When $X=0$, Eq. (B13) gives the same result as Eq. (A10).

[1] G. I. Budker, G. I. Dimov, and V. G. Dudnikov, in *Proceedings of the International Symposium on Electron and Positron Storage Rings, Saclay, 1966* (Universitaires de France, Orsay, 1966), p. VIII-6-1.

[2] H. G. Hereward, CERN Report No. 71-15, 1971 (unpublished).

[3] E. Keil and B. Zotter, CERN Report No. CERN-ISR-TH/71-58, 1971 (unpublished).

[4] D. Neuffer, E. Colton, D. Fitzgerald, T. Hardek, R. Hutson, R. Macek, M. Plum, Henry A. Thiessen, and T. S. Wang, Nucl. Instrum. Methods Phys. Res. A **321**, 1 (1992).

[5] R. J. Macek, A. Browman, D. Fitzgerald, R. C. McCrady, F. E. Merrill, M. A. Plum, T. Spickermann, T. S. Wang, K. C. Harkay, R. Kustom, R. A. Rosenberg, J. E. Griffin, K. Y. Ng, and D. Wildman, in *Proceedings of the Particle Accelerator Conference, Chicago, 2001* (IEEE, Piscataway, NJ, 2001), p. 688.

[6] M. Blaskiewicz, in *Workshop on Instabilities of High Intensity Hadron Beams in Rings*, edited by T. Roser and S. Y. Zhang, AIP Conf. Proc. No. 496 (AIP, Melville, NY, 1999), p. 321.

[7] M. Izawa, Y. Sato, and T. Toyamasu, Phys. Rev. Lett. **74**, 5044 (1995).

[8] K. Ohmi, Phys. Rev. Lett. **75**, 1526 (1995).

[9] H. Fukuma, *Proceedings of ECLOUD'02*, edited by G. Rumolo and F. Zimmerman (CERN, Geneva, 2002), pp.1–10.

[10] Sam Heifets (unpublished), http://www.aps.anl.gov/conferences/icfa/two-stream.html

[11] Z. Y. Guo, H. Huang, S. P. Li, D. K. Liu, L. Ma, Q. Qin, L. F. Wang, J. Q. Wang, S. H. Wang, C. Zhang, F. Zhou, Y. H. Chin, H. Fukuma, S. Hiramatsu, M. Izawa, T. Kasuga, E. Kikutani, Y. Kobayashi, S. Kurokawa, K. Ohmi, Y. Sato, Y. Suetsugu, M. Tobiyama, K. Yokoya, and X. L. Zhang, KEK Report No. 98-23, 1998 (unpublished); in *Proceedings of the First Asian Particle Accelerator Conference, Tsukuba, Japan, 1998*, edited by Y. H. Chin, M. Kihara, H. Kobayashi, N. Akasaka, K. Nigorikawa, and M. Tobiyama (KEK, Tsukuba, 1998), pp. 432–434.

[12] J. M. Jiménez, G. Arduini, P. Collier, G. Ferioli, B. Henrist, N. Hilleret, L. Jensen, K. Weiss, and F. Zimmermann, LHC Project Report No. 632, 2003 (unpublished).

[13] K. Cornlis, in *Proceedings of ECLOUD'02* (Ref. [9]), pp. 11–16.

[14] O. Grőbner, in *Proceedings of the 10th International Accelerator Conference, Protvino, Russia, 1977* (Institute of High Energy Physics, Protvino, 1977), p. 277.

[15] O. Grőbner, in *Proceedings of the 17th IEEE Particle Accelerator Conference (PAC 97), Vancouver, Canada* (IEEE, Piscataway, NJ, 1998), p. 3589.

[16] R. Macek, PSR Technical Note No. PSR-00-10, 2000 (unpublished); V. Danilov, A. Aleksandrov, J. Galambos, D. Jeon, J. Holmes, and D. Olsen, *Workshop on Instabilities of High Intensity Hadron Beams in Rings* (Ref. [6]), p. 315.

[17] M. Blaskiewicz, M. A. Furman, and M. Pivi, Phys. Rev. ST Accel. Beams **6**, 014203 (2003).

[18] J. Wei and R. J. Macek, in *Proceedings of ECLOUD'02* (Ref. [9]), pp. 29–40.

[19] L. F. Wang, H. Fukuma, K. Ohmi, S. Kurokawa and K. Oide, F. Zimmermann, Phys. Rev. ST Accel. Beams **5**, 124402 (2002).

[20] M. T. F. Pivi and M. A. Furman, Phys. Rev. ST Accel. Beams **6**, 034201 (2003).

[21] K. Ohmi, T. Tama, and C. Ohmori, Phys. Rev. ST Accel. Beams **5**, 114402 (2002).

[22] M. A. Furman and M. T. F. Pivi, LBNL 52872 Note No. 516, 2003 (unpublished).

[23] M. A. Furman and M. T. F. Pivi, Phys. Rev. ST Accel. Beams **5**, 124404 (2002).

[24] H. Bruining, *Physics and Applications of Secondary Electron Emission* (Pergamon, New York, 1954).

[25] P. A. Redhead, J. P. Hobson, and E. V. Kornelsen, *The Physical Basis of Ultrahigh Vacuum* (Chapman and Hall, London, 1968), Chap. 4 (reprinted by AIP in 1993 as part of the American Vacuum Society Classics series).

[26] H. Seiler, J. Appl. Phys. **54**, R1 (1983).

[27] R. Cimino *et al.*, Phys. Rev. Lett. **93**, 014801 (2004).

[28] A. V. Fedotov, J. Wei, and R. L. Gluckstern, in *Proceedings of the Particle Accelerator Conference* (Ref. [5]), p. 2851.

[29] R. J. Macek, LANL PSR Technical Note No. PSR-98-04, 1998 (unpublished).

[30] R. J. Macek, in *Proceedings of ECLOUD'02* (Ref. [9]), pp. 259–268.

[31] M. Plum, D. Johnson, R. Macek, F. Merrill, and B. Prichard, LANL PSR Technical Report No. PSR-97-19, 1997 (unpublished).

[32] K. Ohmi and F. Zimmermann, Phys. Rev. Lett. **85**, 3821 (2000).

[33] The data collection was done by detector ED42Y in LANL PSR, 2 July 2002, and is documented in Log Book 95, pp. 6–7. Courtesy R. Macek.

[34] K. Y. Ng *et al.*, in *Proceedings of the Particle Accelerator Conference* (Ref. [5]), p. 2890.

[35] B. Houssais, Thesis, Université de Rennes, France, 1967.

[36] A. Browman (unpublished), http://www.aps.anl.gov/conferences/icfa/two-stream.html

[37] R. Macek (unpublished), http://physics.indiana.edu/∼shylee/ap/mwapc/epfeedback.html

[38] R. Macek, M. Borden, A. Browman, D. Fitzgerald, T. S. Wang, T. Zaugg, K. Harkay, and R. A. Rosenberg, in *Proceedings of the 2003 Particle Accelerator Conference (PAC 03), Portland, Oregon* (IEEE, Piscataway, NJ, 2003).

[39] The data were collected in 7 October 2001 for a sweeping detector of PSR and are documented in Log Book 98, pp. 132–133. Courtesy of R. Macek and A. Browman.

[40] F. Lapique and F. Piuz, Nucl. Instrum. Methods **175**, 297 (1980).

[41] R. Macek, (unpublished), http://www.c-ad.bnl.gov/icfa/

[42] L. F. Wang, H. Fukuma, S. Kurokawa, and K. Oide, Phys. Rev. E **66**, 036502 (2002).

[43] L. F. Wang, D. Raparia, J. Wei, and S. Y. Zhang, Phys. Rev. ST Accel. Beams **7**, 034401 (2004).

[44] Jie Wei, Rev. Mod. Phys. **75**, 1383 (2003).

[45] B. Lehnert, in *Progress in Nuclear Energy*, edited by J. L. Tuck, Series XI, Vol. II (Pergamon, Oxford, 1962).